Enhanced Average-Value Modeling of Interleaved DC–DC Converters Using Sampler Decomposition

Alejandro Villarruel-Parra, *Member, IEEE*, and Andrew J. Forsyth, *Senior Member, IEEE*

***Abstract*—To provide a basis for controller design in interleaved dc–dc converters, an improved small-signal averaged model is presented. Sampler decomposition techniques are used to represent the interleaved operation of the individual control loops within the converter. The resultant model reveals interaction effects and instability phenomena that are not predicted by a simple noninterleaved model, and which impose significant restrictions on the selection of control parameters. The model is validated by detailed simulations and experimental results from a digitally controlled dual-interleaved boost converter.**

***Index Terms*—Average current, control, dc–dc converters, interleaved converters, modeling, small signal.**

I. Introduction

INTERLEAVED dc–dc converters have been widely adopted in power supplies for microprocessors and communication systems, high-power-factor rectifiers, and more recently in the power train of electric vehicles. The parallel-connected channels of an interleaved converter, Fig. 1, use the same topology, component values, and switching frequency, but their switching cycles are mutually delayed, providing ripple cancellation at input and output. With two interleaved channels, the switching delay is half the switching period, the input and output ripple frequency is doubled, and the ripple-current amplitude is reduced, allowing smaller filter capacitors to be used. Also, the current is distributed across multiple devices and components, reducing thermal load. For instance, the dual-interleaved boost converter, Fig. 2, is one of the topologies that has been proposed to interface fuel-cells, supercapacitors, battery banks, and traction drives within the power train of an electric vehicle [1]–[3], where power levels could be up to 100 kW. The circuit in Fig. 2 uses an interphase transformer to combine the voltages of the two switching legs and a single inductor, and is considered to offer a reduced magnetic component weight compared with a two-inductor alternative [4].

To prevent current imbalances between parallel phases, for example, due to second-order effects, such as mismatches in switching times and circuit impedances, some form of current control is normally required in interleaved converters. With a small number of phases, peak or averaged current-mode control can be used for each phase, with a common current reference formed by the output voltage control loop. Some of the solutions to balance the phase currents for systems with a high number of phases include: operating the parallel converters in discontinuous-conduction mode, [3]; balancing the phase-currents using digital algorithms, [5], [6]; and nonlinear control methodologies [7].

Averaging techniques have been used by several authors for the dynamic analysis and control design of interleaved converters, for example, state-space averaging and circuit averaging [8]–[12]; however, these approaches do not account for the interleaved operation of the converter phases, creating the possibility that unexpected interactions and instability phenomena could occur. For instance, the stability analysis carried out in [13] for a dual-interleaved buck converter demonstrated using

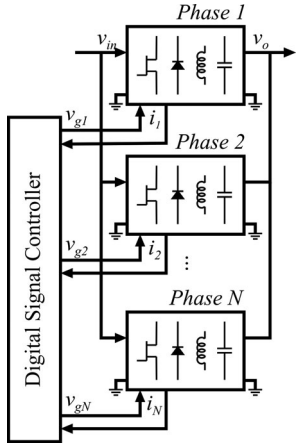

Fig. 1. Interleaved dc–dc converter.

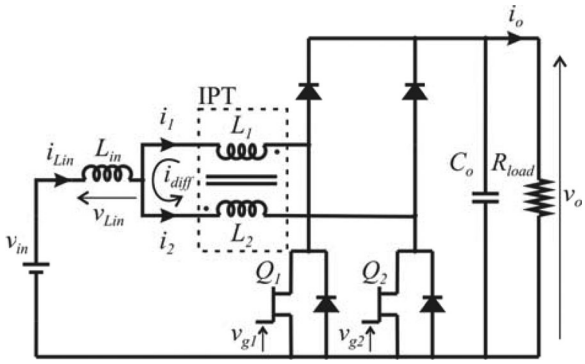

Fig. 2. Dual-interleaved boost converter with interphase transformer.

Manuscript received November 29, 2015; revised February 3, 2016 and March 25, 2016; accepted April 11, 2016. Date of publication April 27, 2016; date of current version December 9, 2016. Recommended for publication by Associate Editor L. Corradini.

A. Villarruel-Parra was with the School of Electrical and Electronic Engineering, The University of Manchester, Manchester M13 9PL, U.K. He is now also with the School of Mechanical and Electrical Engineering, National Polytechnic Institute, Mexico City 04430, Mexico (e-mail: vipaal.22@gmail.com).

A. J. Forsyth is with the School of Electrical and Electronic Engineering, The University of Manchester, Manchester M13 9PL, U.K. (e-mail: andrew.forsyth@manchester.ac.uk).

Color versions of one or more of the figures in this paper are available online at http://ieeexplore.ieee.org.

Digital Object Identifier 10.1109/TPEL.2016.2559449

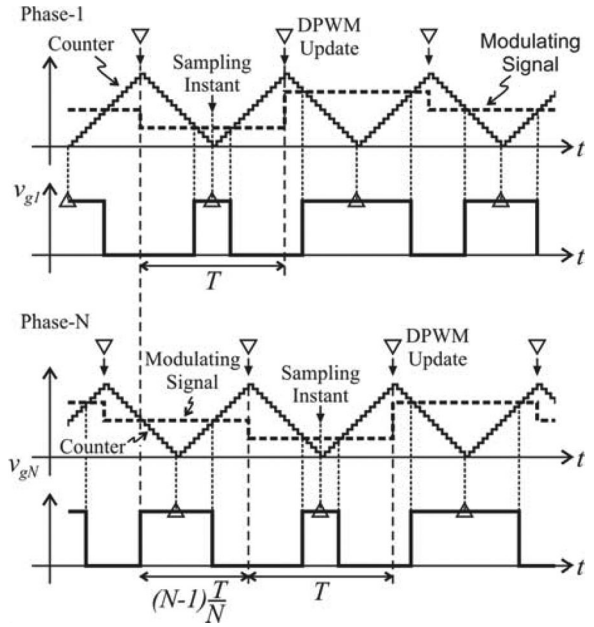

Fig. 3. Control waveforms of an interleaved dc–dc converter with digital average-current control.

nonlinear maps that slow-scale instabilities arise in the system due to the interaction of the converter phases, which are not predicted by an averaged model. Sampled-data techniques provide an alternative to averaged models, they incorporate both slow-scale and switching-frequency-related fast-scale effects and can include interleaved operation [14]; however, the analysis complexity makes these models very difficult to use in many cases.

In this paper, multirate data-sampled theory is used to enhance the small-signal averaged model of interleaved converters to include the interactions of the converter phases, and provide a theoretical basis for the direct digital design of the current control loops. The modeling technique is initially presented in a general fashion for an *N*-phase average current-mode-controlled converter. Based on this theory, a modeling example is presented for a dual-interleaved boost converter with interphase transformer. The model is validated using time-domain simulations and practical results from a multikilowatt prototype, showing how the interleaved operation introduces instability regions that are not predicted by a noninterleaved averaged model.

II. Small-Signal Modeling of Interleaved Converters With Average-Current Mode Control

A. Operation of Interleaved Converters Using Digital Average-Current Mode Control

To ensure an equal distribution of the current amongst the converter phases, a separate current feedback loop per converter is typically used as illustrated in Fig. 1. A number of digital current control methods for single-phase dc–dc converters have been proposed in the literature, showing that by strategic synchronization of the current sampling instants with specific events of the digital pulse width modulator (PWM) it is possible to acquire the peak current, valley-current, or the average current in each feedback loop [15]. Fig. 3 shows waveforms to illustrate the sampling of the average current. The digital PWM counter is configured in count up-down mode, generating a triangular waveform. The digital modulator output is turned-on when the counter crosses the modulating signal during the count down. In contrast, when the counter crosses the modulating waveforms during the count up, the output signal is turned-off. The modulating signal is updated once per cycle when the counter reaches its maximum value; therefore, the switching instants of the PWM output waveforms are symmetrical with respect to the minimum value of the digital triangular waveform. From this symmetry, it follows that if the feedback current sampling occurs when the counters are at their minimum value; the current sample will be located in the middle of the transistor conducting periods and will be the local-average value of the phase current. This method is termed triangular-carrier modulation with symmetric on-time [15], [16]. To achieve the interleaving of the PWM waveforms for each converter, the digital counters of the feedback loops are delayed with respect to each other by *T/N*, where *T* is the switching period and *N* is the number of phases.

B. Closed-Loop Small-Signal Model of the System

Fig. 4 shows the block diagram of an average current-mode-controlled interleaved converter, assuming that the converter and controller can be represented by linear transfer functions. Each converter phase is represented by an averaged linearized transfer function which relates small changes in the transistor duty ratios $\tilde{d}_1(s), \tilde{d}_2(s), \ldots, \tilde{d}_N(s)$ to the small changes in the phase currents $\tilde{i}_1(s), \tilde{i}_2(s), \ldots, \tilde{i}_N(s)$. The analog-to-digital conversion of the phase currents is modeled by the sampler devices $S_1, S_2, \ldots, S_N$ which operate in an interleaved manner. Since both the reference and phase currents in each feedback loop are sampled synchronously, a single sampler located after the summing junctions is used. The quantization nonlinearity of the ADC and the measurement and conditioning delays are disregarded. The digital compensators on each phase, $C(z)$, are represented in the Laplace domain using the transfer function $C(s)$ followed by the corresponding phase sampler. The delay associated with the digital compensator, $e^{-\tau s}$, is identical for each control loop. Finally, the digital modulator operation is represented by the zero-order-hold extrapolator transfer function [15], [17]

$$G_{h0}(s) = \frac{\left(1 - e^{-sT}\right)}{s}. \tag{1}$$

This representation may be replaced by more elaborate small-signal models such as that introduced in [15].

C. Modeling of the Interleaved Operation of the Feedback Loops

Assuming the sampler S_1 in Fig. 4 as the reference, the delayed samplers S_2 to S_N may be represented in terms of S_1 preceded by a time-advance unit of $+n(T/N)$ and followed by a time-delay unit of $-n(T/N)$, where $n = 1,2,\ldots,(N-1)$, as illustrated in Fig. 5. This technique is known as the sampler decomposition method [17], [18]. Upon substitution of the

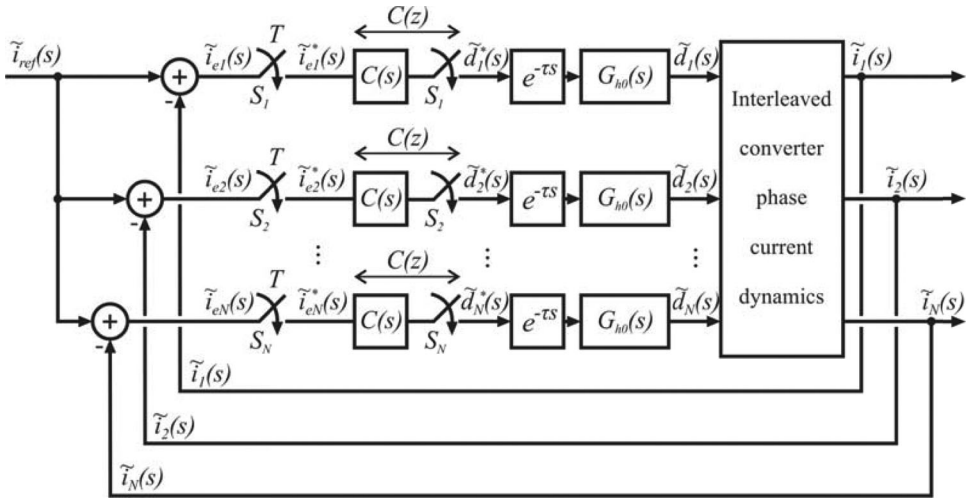

Fig. 4. Block diagram of a digital average-current mode controlled interleaved dc–dc converter.

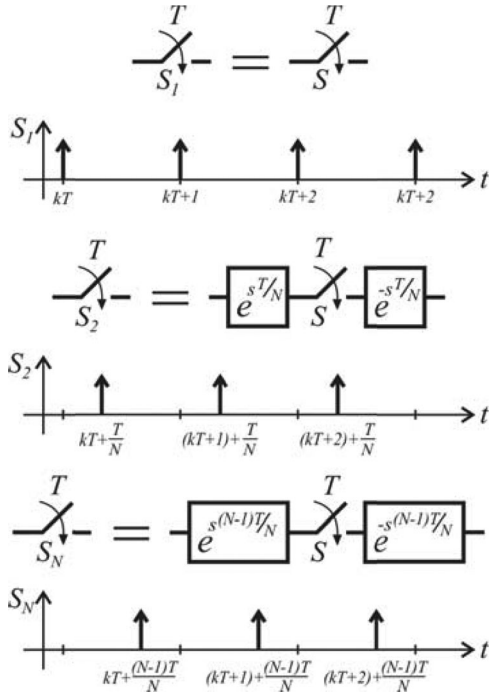

Fig. 5. Equivalent sampler representation using the sampler decomposition technique.

equivalent samplers in Fig. 4, the system may be analysed using z-transforms.

III. Modeling Example: Dual-Interleaved Boost Converter With Interphase Transformer

A. Small-Signal Averaged Model of the Power Stage

Fig. 2 shows the schematic diagram of the dual-interleaved boost converter with IPT. By substitution of the converter switch networks with the averaged PWM switch model, the dc and averaged small-signal model of the converter shown in Fig. 6 is obtained, where the IPT has been modeled using self- and mutual-inductances. Using Fig. 6, the small-signal model of the converter can be represented in the state-space form as

$$\dot{\tilde{\mathbf{x}}} = \mathbf{A_{av}}\tilde{\mathbf{x}} + \mathbf{B_{av}}\tilde{\mathbf{u}} \tag{2}$$

where the state vector, $\tilde{\mathbf{x}}$, comprises the small-signal components of the phase currents in the IPT windings and the voltage across the output capacitor: $\tilde{\mathbf{x}} = [\tilde{i}_1, \tilde{i}_2, \tilde{v}_o]^T$; and the input vector, $\tilde{\mathbf{u}}$, contains the control inputs for each phase and the load disturbance current: $\tilde{\mathbf{u}} = [\tilde{d}_1, \tilde{d}_2, \tilde{i}_z]^T$. The matrices $\mathbf{A}_{\rm av}$ and $\mathbf{B}_{\rm av}$ in (2) may be expressed as

$$\mathbf{A_{av}} = \begin{bmatrix} -\dfrac{R_{\rm in}(L_c+L_m)}{L_{\rm Tot}} & -\dfrac{R_{\rm in}(L_c+L_m)}{L_{\rm Tot}} & -\dfrac{(1-D)(L_c+L_m)}{L_{\rm Tot}} \\ -\dfrac{R_{\rm in}(L_c+L_m)}{L_{\rm Tot}} & -\dfrac{R_{\rm in}(L_c+L_m)}{L_{\rm Tot}} & -\dfrac{(1-D)(L_c+L_m)}{L_{\rm Tot}} \\ \dfrac{(1-D)}{C_o} & \dfrac{(1-D)}{C_o} & -\dfrac{1}{R_{\rm load}C_o} \end{bmatrix} \tag{3}$$

$$\mathbf{B_{av}} = \begin{bmatrix} \dfrac{V_{\rm in}(L_{\rm in}+L_c)}{L_{\rm Tot}(1-D)} & -\dfrac{V_{\rm in}(L_{\rm in}-L_m)}{L_{\rm Tot}(1-D)} & 0 \\ -\dfrac{V_{\rm in}(L_{\rm in}-L_m)}{L_{\rm Tot}(1-D)} & \dfrac{V_{\rm in}(L_{\rm in}+L_c)}{L_{\rm Tot}(1-D)} & 0 \\ -\dfrac{V_{\rm in}}{2R_{\rm load}C_o(1-D)^2} & -\dfrac{V_{\rm in}}{2R_{\rm load}C_o(1-D)^2} & \dfrac{1}{C_o} \end{bmatrix} \tag{4}$$

where $L_c = L_1 = L_2, L_m$ is the mutual inductance between L_1 and L_2, and $L_{\rm Tot} = 2L_{\rm in}(L_c + L_m) + (L_c^2 - L_m^2)$. By transforming into the Laplace domain, the small-signal transfer functions between $\tilde{d}_1(s)$ and $\tilde{d}_2(s)$ and the converter phase-currents, $\tilde{i}_1(s)$ and $\tilde{i}_2(s)$, may be determined in the form

$$\tilde{i}_1(s) = G_{d1i1}(s)\tilde{d}_1(s) + G_{d2i1}(s)\tilde{d}_2(s) \tag{5}$$

$$\tilde{i}_2(s) = G_{d1i2}(s)\tilde{d}_1(s) + G_{d2i2}(s)\tilde{d}_2(s), \tag{6}$$

where $G_{d1i1}(s) = G_{d2i2}(s)$ and $G_{d1i2}(s) = G_{d2i1}(s)$ since the components that comprise the converter phases are assumed identical. The transfer functions $G_{d1i1}(s)$ and $G_{d1i2}(s)$ can be found in the Appendix.

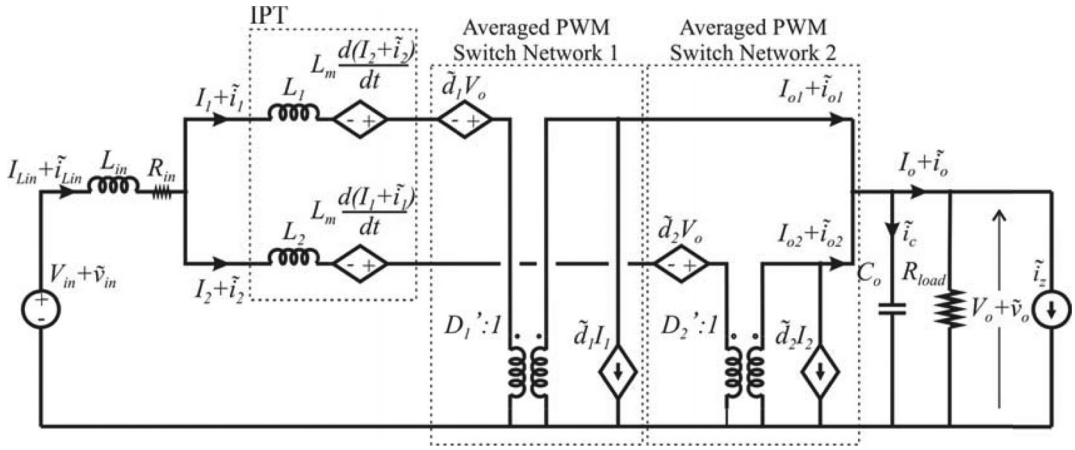

Fig. 6. DC and small-signal model of the dual-interleaved boost converter with IPT.

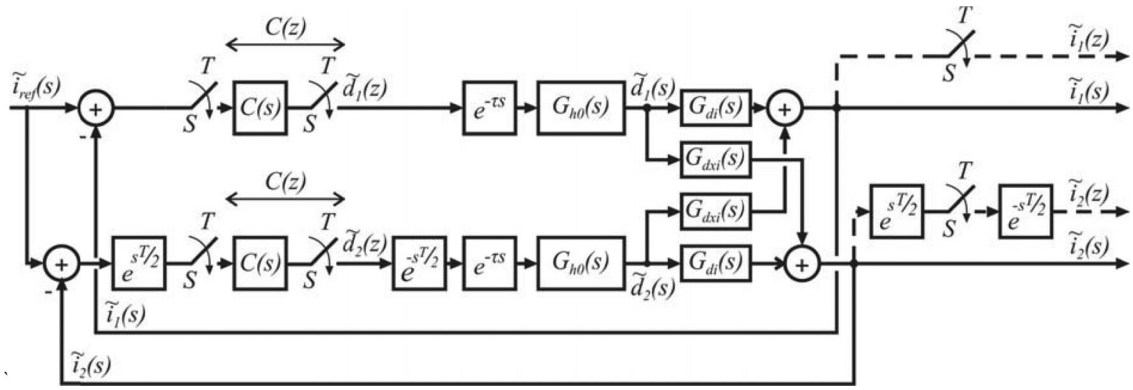

Fig. 7. Block diagram of the dual-interleaved boost converter with IPT with digital average-current control.

B. Small-Signal Averaged Model of the Converter With Current Feedback Control

The closed-loop small-signal model of the dual-interleaved boost converter may be derived from the generalized system diagram in Fig. 3 by substitution of the duty ratio to phase-current transfer functions, (5) and (6), as shown in Fig. 7, where $G_{d1i1}(s) = G_{d2i2}(s) = G_{di}(s)$ and $G_{d1i2}(s) = G_{d2i1}(s) = G_{dxi}(s)$. Furthermore, the sampler S_2 has been replaced by its equivalent representation in terms of S_1 using time advance and time-delay units equal to $e^{+sT/2}$ and $e^{-sT/2}$, as described in Section II. Closed-loop transfer functions for the phase currents $\tilde{i}_1(z)/\tilde{i}_{\rm ref}(z)$ and $\tilde{i}_2(z)/\tilde{i}_{\rm ref}(z)$, may be determined by analysis of Fig. 7. First, considering the two feedback loops, expressions may be written for $\tilde{d}_1(z)$ and $\tilde{d}_2(z)$

$$\begin{aligned}\tilde{d}_1(z) = {} & C(z)\left[Z\left\{\tilde{i}_{\rm ref}(s)\right\}\right. \\ & - \tilde{d}_1(z) Z\left\{e^{-\tau s} G_{h0}(s) G_{di}(s)\right\} \\ & \left. - \tilde{d}_2(z) Z\{e^{-sT/2} e^{-\tau s} G_{h0}(s) G_{dxi}(s)\}\right] \quad (7)\\ \tilde{d}_2(z) = {} & C(z)[Z\{e^{sT/2}\tilde{i}_{\rm ref}(s)\} \\ & - \tilde{d}_1(z) Z\{e^{sT/2} e^{-\tau s} G_{h0}(s) G_{dxi}(s)\} \\ & \left. - \tilde{d}_2(z) Z\left\{e^{-\tau s} G_{h0}(s) G_{di}(s)\right\}\right], \quad (8)\end{aligned}$$

where $Z\{F(s)\}$ denotes the z-transform of $F(s)$. Considering the fictious-sampler outputs in Fig. 7

$$\begin{aligned}\tilde{i}_1(z) = {} & \tilde{d}_1(z) Z\{e^{-\tau s} G_{h0}(s) G_{di}(s)\} \\ & + \tilde{d}_2(z) Z\{e^{-sT/2} e^{-\tau s} G_{h0}(s) G_{dxi}(s)\} \quad (9)\\ \tilde{i}_2(z) = {} & \tilde{d}_1(z) Z\{e^{sT/2} e^{-\tau s} G_{h0}(s) G_{dxi}(s)\} \\ & + \tilde{d}_2(z) Z\left\{e^{-\tau s} G_{h0}(s) G_{di}(s)\right\}. \quad (10)\end{aligned}$$

Eliminating $\tilde{d}_1(z)$ and $\tilde{d}_2(z)$ from (7) and (8) using (9) and (10), the closed-loop transfer functions of the system are obtained (11)–(12), which are shown at the bottom of the next page.

The z-transforms of the constituent transfer functions of (11) and (12) are defined as

$$\begin{aligned}G_{di}(z) = {} & Z\left\{e^{-\tau s} G_{h0}(s) G_{di}(s)\right\} = \\ & Z_m\left\{G_{h0}(s) G_{di}(s)\right\}|_{m=1-(\tau/T)} \quad (13)\\ G_{dxi\phi}(z) = {} & Z\{e^{-sT/2} e^{-\tau s} G_{h0}(s) G_{dxi}(s)\} = \\ & Z_m\left\{G_{h0}(s) G_{dxi}(s)\right\}|_{m=1-(1/2+(\tau/T))} \quad (14)\\ G_{dxi\theta}(z) = {} & Z\{e^{sT/2} e^{-\tau s} G_{h0}(s) G_{dxi}(s)\} = \\ & z\, Z_m\left\{G_{h0}(s) G_{dxi}(s)\right\}|_{m=(1/2-(\tau/T))} \quad (15)\end{aligned}$$

where the z-transform of the transfer functions multiplied by fractional time-delay and time-advance units are evaluated using the modified z-transform method [17].

Inspection of (11) and (12) reveals that an open-loop transfer function is not immediately identifiable, complicating the use of traditional compensator design procedures such as Bode plots. Following a similar method, the closed-loop transfer functions may also be derived assuming synchronous operation of the samplers S_1 and S_2 in Fig. 7, resulting in

$$G_{i1i\mathrm{ref}}(z) = G_{i2i\mathrm{ref}}(z) = \frac{C(z)\left[G_{di}(z) + G_{dxi}(z)\right]}{1 + C(z)\left[G_{di}(z) + G_{dxi}(z)\right]} \tag{16}$$

where

$$G_{dxi}(z) = Z\left\{e^{-\tau s} G_{h0}(s) G_{dxi}(s)\right\} = Z_m\left\{G_{h0}(s) G_{dxi}(s)\right\}|_{m=\tau}. \tag{17}$$

In contrast with the interleaved transfer functions (11) and (12), (16) is greatly simplified and also an open-loop transfer function is easily identifiable.

IV. Comparison Between Interleaved and Noninterleaved Models

A. Performance of the Phase Current to Step Changes

To illustrate the improved accuracy of the interleaved model, a set of small step responses is presented in Fig. 8 for one of the phase currents in a dual-interleaved boost converter. SABER simulation results, using a detailed switched model that includes the interleaved sampling of the phase currents in the digital controller, are shown in the first column, while the second and third columns show the transfer function predictions (11) and (16) from the interleaved and the noninterleaved models, respectively. The SABER and small-signal models exclude all losses except R_{in}, the series resistance of the input inductor. The converter parameters are listed in Table I and the same values are used for the practical validation in Section V. In the first row in Fig. 8, the PI compensator integral gain is varied from 1 to 20, in the second row, the steady-state phase-current is increased from 40 to 120 A; finally, in the last row, the input voltage is varied from 40 to 150 V.

The results from the transfer functions show a close correspondence with the simulation results with virtually-identical rise time natural frequency (5 kHz) and damping ratio. However, a lower lightly damped natural frequency (approximately 850 Hz) is evident in many of the responses from the interleaved model, but is completely absent in the noninterleaved model results. The same natural frequency is also observable in the SABER results. The top set of responses in Fig. 8 with integral gain $K_i = 20$ show unstable behavior in the SABER simulation and interleaved model, while the noninterleaved model is completely stable. The lower frequency natural mode in the i_1 phase current was found to occur in antiphase in the i_2 phase current, but was unobservable in the input inductor current. The additional high-frequency oscillations that occur in the SABER simulation results were attributed to PWM quantization and current-sampling effects.

B. Pole-Zero Maps and Frequency Response

To compare the transfer functions obtained from the proposed interleaved model and the standard noninterleaved model, z-domain pole-zero maps are shown in Fig. 9 for the closed-loop reference-to-phase-1 current transfer function for the operating condition of $V_{\mathrm{in}} = 80$ V, $I_{\mathrm{in}} = 200$ A, and $R_{\mathrm{load}} = 5.2\ \Omega$ with PI controller gains $K_p = 10(T)$ and $K_i = 15$. This operating condition corresponds with the plot labeled Point A in Fig. 8. The main difference between the plots is that the interleaved model contains an additional pair complex poles, which are just inside the unit circle and cancelled by complex zeros, indicating a natural mode that is unobservable in the phase-current transfer function. The natural frequency of the poles is around 850 Hz and they are responsible for the lightly damped oscillation in the transient responses in Fig. 8.

Finally, Fig. 10 shows the closed-loop reference-to-phase-1 current frequency response from the interleaved model compared with the result from a SABER switched simulation obtained using the SABER time-domain system analyser tool. The same parameters were used for the pole-zero maps in Fig. 9. In general, the two sets of data correspond closely, providing further validation of the model; however, the cancelled complex poles are much less evident in the SABER results.

C. Root-Loci of the System and Stability Maps

To provide further insight into the system dynamics and stability, the sensitivity of the system poles to parameter variations was examined using (11) and (12). The parameters included the input-voltage load-resistance and PI compensator gains.

Fig. 11(a) shows the trajectories of the system poles when D is varied from 0.2 to 0.8 for values of K_i of 1, 10, and 20, while the proportional gain is fixed at $K_p = 10(T)$. The plot shows a pair of low-frequency complex poles located in the vicinity of the $+1$ point, which are not present in the noninterleaved model of the system (16), and are attributed to the squared term of the compensator transfer function found in the denominator of (11) and (12). Also, a pair of high-frequency complex poles

$$G_{i1i\mathrm{ref}}(z) = \frac{\tilde{i}_1(z)}{\tilde{i}_{\mathrm{ref}}(z)} = \frac{C(z)G_{di}(z) + C(z)G_{dxi\phi}(z) + C^2(z)\left[G_{di}^2(z) - G_{dxi\phi}(z)G_{dxi\theta}(z)\right]}{1 + 2C(z)G_{di}(z) + C^2(z)\left[G_{di}^2(z) - G_{dxi\phi}(z)G_{dxi\theta}(z)\right]} \tag{11}$$

$$G_{i2i\mathrm{ref}}(z) = \frac{\tilde{i}_2(z)}{\tilde{i}_{\mathrm{ref}}(z)} = \frac{C(z)G_{di}(z) + C(z)G_{dxi\theta}(z) + C^2(z)\left[G_{di}^2(z) - G_{dxi\phi}(z)G_{dxi\theta}(z)\right]}{1 + 2C(z)G_{di}(z) + C^2(z)\left[G_{di}^2(z) - G_{dxi\phi}(z)G_{dxi\theta}(z)\right]} \tag{12}$$

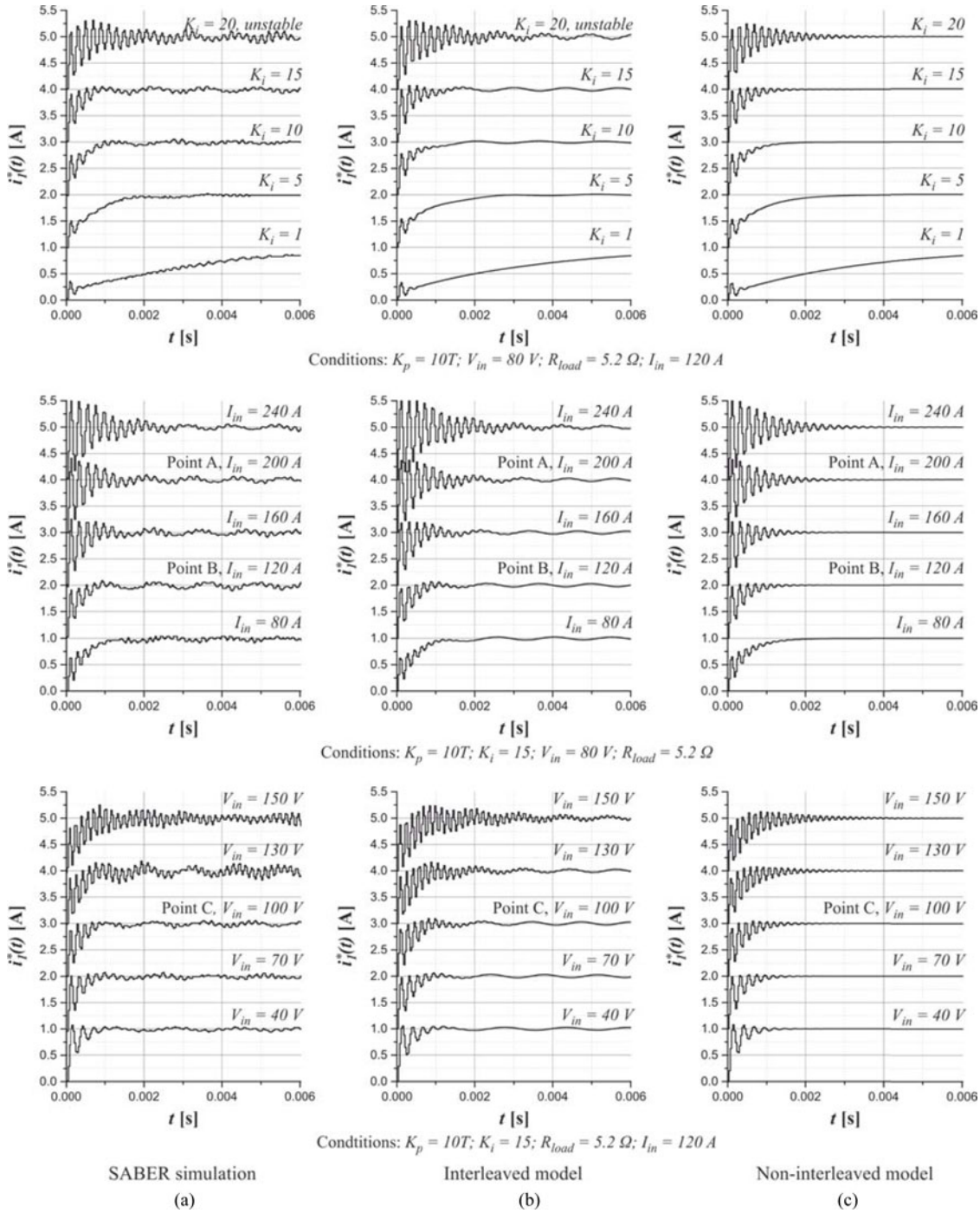

Fig. 8. Time-domain response of the phase-*1* current of the (a) SABER switched model, (b) the interleaved small-signal model, and (c) the noninterleaved/conventional small-signal model to small step-increments in the reference input.

can be identified in the root locus, which were also observed in the root locus of the noninterleaved model. As the duty ratio is increased, the high-frequency poles tend to move around the unit circle, with $K_i = 1$ the poles move toward the real axis, but with higher values of K_i, for example, $K_i = 20$, the poles turn back on themselves and move outside the unit circle. The low-frequency complex poles, on the other hand, tend to move around the unit circle and away from the real axis, in the case of $K_i = 20$, the poles lie on the unit circle, but are inside the unit circle with lower values of K_i. Fig. 11(b) shows a similar pattern in the pole trajectories for different input voltages. The high-frequency poles tend to become unstable for higher input voltages and higher duty ratios, while the low-frequency poles remain close to the unit circle.

The significant difference in the converter stability range predicted by the interleaved and noninterleaved models is

TABLE I
CONVERTER COMPONENTS AND PARAMETERS

Component	Symbol	Value
Input Inductance	$L_{\rm in}$	5.12 μH
Input inductor stray resistance	$R_{\rm in}$	0.029 Ω
IPT self-inductance	L_1, L_2	75.14 μH
IPT mutual inductance	L_m	74.9 μH
IPT coupling coefficient	k	0.997
Output capacitance	C_o	45 μF
Switching frequency	f	30 kHz
Switching/sampling period	T	33.33 μs
Computational delay	τ	T/2

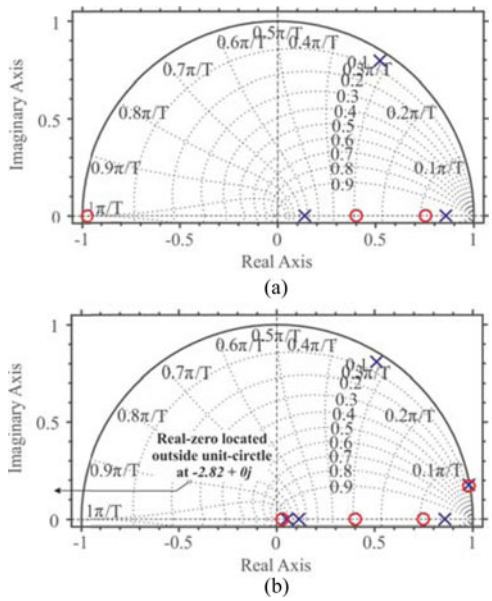

Fig. 9. Pole-zero maps from the closed-loop, reference-to-phase-*1* current transfer function, $G_{i1i{\rm ref}}(z)$, from (a) the noninterleaved small-signal model, and (b) the interleaved small-signal model. $V_{\rm in} = 80$ V, $I_{\rm in} = 200$ A, and $R_{\rm load} = 5.2\ \Omega$ corresponding to Point A, Fig. 8. $K_p = 10(T)$ and $K_i = 15$.

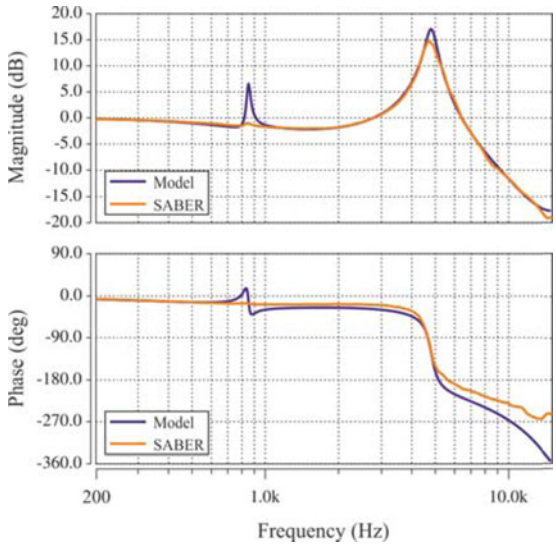

Fig. 10. Comparison of the frequency response of the closed-loop, reference-to-phase-*1* current transfer function, $G_{i1i{\rm ref}}(z)$, obtained from the interleaved small-signal model and the switched simulation. $V_{\rm in} = 80$ V, $I_{\rm in} = 200$ A, and $R_{\rm load} = 5.2\ \Omega$ corresponding to Point A, Fig. 8. $K_p = 10(T)$ and $K_i = 15$.

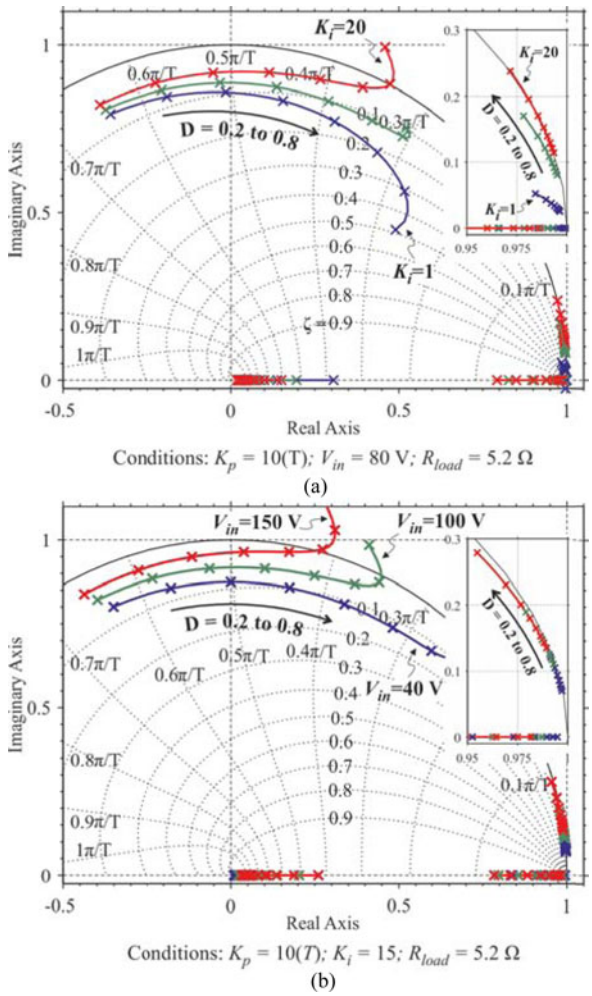

Fig. 11. Sensitivity of the pole trajectories from the interleaved model to variations in (a) the integral gain, $K_i = 1$, 10, and 20; and (b) the input voltage $V_{\rm in} = 40$ V, 100 V, and 150 V.

illustrated by the shaded regions in the K_p/K_i controller design space Fig. 12. The dark shaded regions indicate the stable combinations of K_p and K_i predicted by the interleaved model, while the lighter shaded areas are the additional regions where the noninterleaved/conventional model suggests that the system operation will be stable. The regions were generated numerically by calculation of the system poles over a systematic sweep of the controller parameters using (11) and (16). The plots indicate that the conventional model seriously over predicts the converter stability limits, particularly for higher values of K_i and lower values of K_p.

V. EXPERIMENTAL PROTOTYPE AND MODEL VALIDATION

Experimental validation of the interleaved converter model was undertaken using a multikilowatt dual-interleaved boost converter with IPT, Fig. 2, which had been developed for an electric vehicle application. The IGBT-based converter operated at 30 kHz with output voltages up to 250 V. A Texas Instruments TMS320F28335 was used to implement the

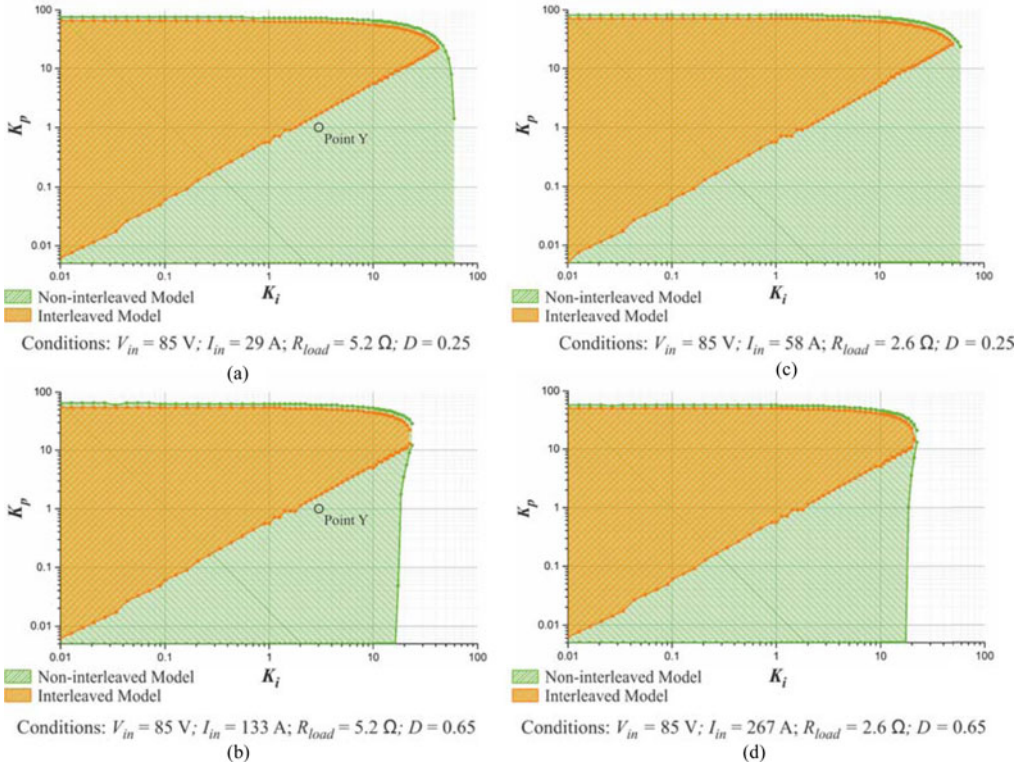

Fig. 12. Comparison of the stability range predicted by the interleaved and the conventional/noninterleaved model when a digital PI compensator is used to regulate the current-feedback control loops at different points of operation.

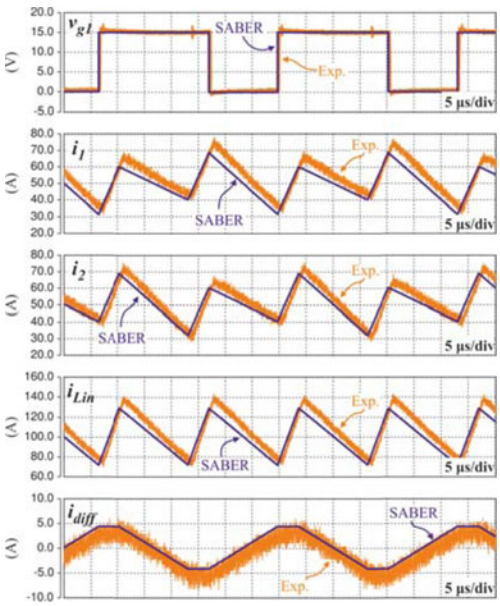

Fig. 13. Simulated and experimental waveforms of the DIBC with IPT under steady-state conditions. $V_{\rm in} = 80$ V, $R_{\rm load} = 5.2\ \Omega$, $I_{\rm in} = 100$ A, $D = 0.61$, $V_o = 205$ V, and $P_o = 8$ kW.

digital interleaved phase current control and PWM generation. The phase currents were measured using Hall-effect sensors, and the system operated without an output voltage control loop. The converter parameters are listed in Table I, and are identical to the values used in the simulations and predictions in Section IV. Fig. 13 shows a comparison of the steady-state waveforms v_{g1}, i_1, i_2, i_L, and $i_{\rm diff}$ (calculated as $(i_2 - i_1)/2$) obtained from the simulation and the experimental test rig which confirm the accuracy of the simulation results. Small-signal step responses (15%) in the current reference, $i_{\rm ref}$, were used to examine the transient behavior of the prototype and to compare with SABER simulations and predictions from the interleaved model. Fig. 14 shows results for two operating conditions with experimental data in the upper plots and SABER simulations and model predictions in the lower plots. The two operating conditions correspond with the plots labeled Point B and Point C in Fig. 8. The three sets of data correspond closely for both operating points. The high-frequency natural mode (5 kHz) is clearly visible and its damping is accurately predicted; furthermore, the lightly damped low-frequency natural mode (880 Hz approximately) is clearly evident in all the datasets, confirming the accuracy of the interleaved model.

Fig. 15 shows the experimental and simulation results of switching the converter into an unstable operating condition. Initially in Fig. 15, a stable combination of K_p and K_i was used, then at $t = 30$ ms, the gains were changed to $K_p = 1(T)$ and $K_i = 3$. The values are marked as Point Y in Fig. 12 and are predicted to be unstable by the interleaved model but should be stable according to the noninterleaved analysis. The results show that the phase current becomes unstable after the change of gains and validates the prediction of the interleaved model.

Finally, Fig. 16 shows large-signal reference current step responses from the converter along with SABER simulations. The digital phase current controllers were designed using the interleaved model, root-locus plots, and stability maps to ensure well-damped responses over the converter operating range. The

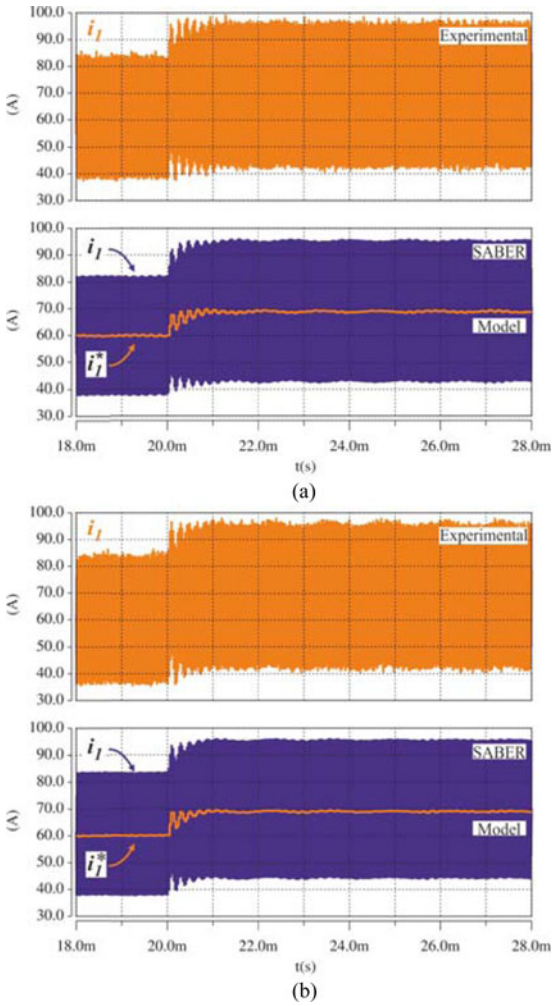

Fig. 14. Experimental and simulated response of i_1 to a 15% step increase in $I_{\rm ref}$ going from 60 to 69 A for (a) $V_{\rm in} = 100$ V corresponding to Point C, Fig. 8; and (b) $V_{\rm in} = 80$ V corresponding to Point B, Fig. 8. $R_{\rm load} = 5.2\ \Omega$, $I_{\rm in} = 120$ A, $K_p = 10(T)$, and $K_i = 15$.

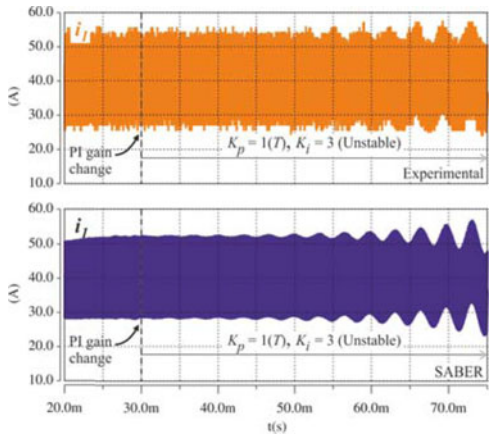

Fig. 15. Experimental and simulated response of i_1 to an unstable set of K_p and K_i gains predicted by the interleaved model. $V_{\rm in} = 85$ V, $R_{\rm load} = 5.2\ \Omega$, $I_{\rm in} = 80$ A corresponding to Point Y, Fig. 10. Initial PI gains: $K_p = 10(T)$ and $K_i = 3$.

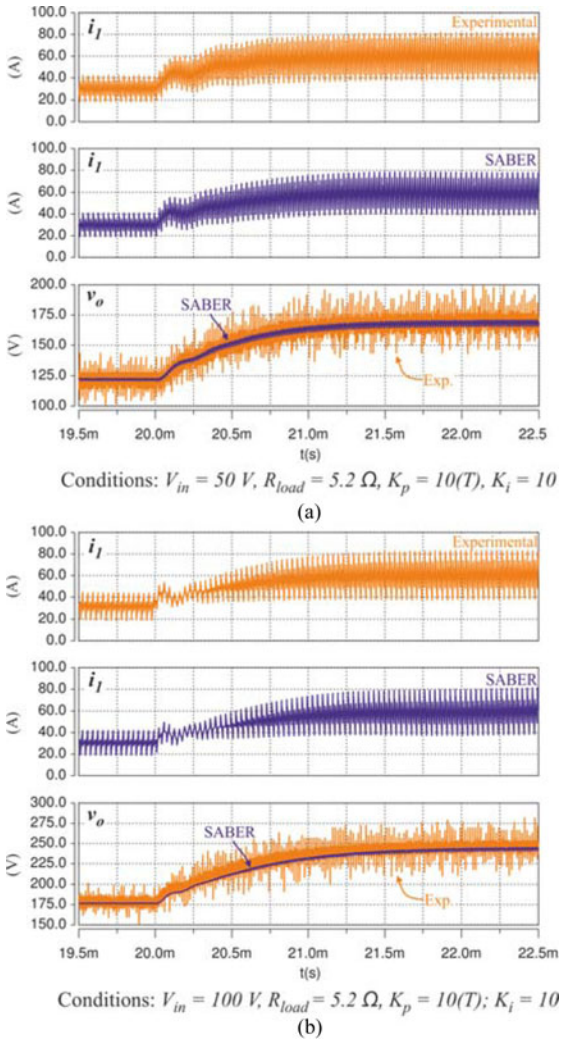

Fig. 16. Simulated and experimental response of i_1 and v_o to a step increase in $I_{\rm ref}$ going from 30 to 60 A for (a) $V_{\rm in} = 50$ V and (b) $V_{\rm in} = 100$ V.

selected control parameters were $K_p = 10(T)$ and $K_i = 10$. Apart from confirming the effectiveness of the model, the results also confirmed that the phase currents are well-balanced throughout the transient preventing any possibility of IPT saturation. While the response times of the phase currents (around 1 ms) are much slower than could be achieved with an analogue current mode controller, these could be improved through optimization of the digital implementation, in particular by reducing the processing delay in the update of the PWM signals.

VI. Conclusion

Using the sampler decomposition technique, a small-signal averaged model for average current-mode controlled, interleaved converters that accounts for the interleaved interaction of the phases has been developed. The method was applied to a dual-interleaved boost converter with interphase transformer and the closed-loop transfer functions were validated using time-domain step responses from a SABER simulation and experimental prototype. The model revealed an instability region that is not predicted by a noninterleaved model and which restricts

the combinations of controller gains that may be used. The instability was attributed to the presence of a low-frequency natural mode that is virtually unobservable in the phase current transfer functions. The model was successfully used in the design of the phase current controllers for the interleaved boost converter, the large-signal response times of the currents being around 1 ms. Furthermore, the phase currents remained well-balanced at all times.

The analysis and design approach is based on well-known averaged converter models and may be readily applied to other circuit topologies such as dual-interleaved converters with separate inductors and no interphase transformer, and to systems with a greater number of phases. While sampled-data techniques could be used to analyze interleaved sampling effects in these converters, [14], the comparative simplicity of the proposed modeling method is seen as a great advantage; however, as it is based on averaging, the model is limited to the prediction slow-scale dynamics.

APPENDIX
SMALL-SIGNAL CONTROL-TO-PHASE CURRENT TRANSFER FUNCTIONS OF THE DIBC WITH IPT

$$G_{d1i1}(s) = G_{d2i2}(s) =$$

$$G_{di}(s) = \left[\frac{(L_c + L_{\rm in})\,V_{\rm in}}{(1-D)L_{\rm Tot}}\right]\frac{\left(s^2 - a_{di1}\,s + a_{di0}\right)}{s\left(s^2 + b_1\,s + b_0\right)} \tag{A.1}$$

$$a_{di1} = \frac{\left((3L_c + 2L_{\rm in} + L_m)\,L_{\rm Tot} + 2C_o\,(L_c + 2L_{\rm in} - L_m)\,(L_c + L_m)\,R_{\rm in}R_{\rm load}\right)}{2C_o\,L_{\rm Tot}R_{\rm load}\,(L_c + L_{\rm in})} \tag{A.2}$$

$$a_{di0} = \frac{(L_c + 2L_{\rm in} - L_m)\,(L_c + L_m)\left(R_{\rm in} + (1-D)^2 R_{\rm load}\right)}{C_o\,L_{\rm Tot}R_{\rm load}\,(L_c + L_{\rm in})} \tag{A.3}$$

$$G_{d1i2}(s) = G_{d2i1}(s) =$$

$$G_{dxi}(s) = \left[-\frac{(L_{\rm in} - L_m)\,V_{\rm in}}{(1-D)L_{\rm Tot}}\right]\frac{\left(s^2 - a_{dxi1}\,s + a_{dxi0}\right)}{s\left(s^2 + b_1\,s + b_0\right)} \tag{A.4}$$

$$a_{dxi1} = \frac{\left((L_c - 2L_{\rm in} + 3L_m)\,L_{\rm Tot} - 2C_o\,(L_c + 2L_{\rm in} - L_m)\,(L_c + L_m)\,R_{\rm in}R_{\rm load}\right)}{2C_o\,L_{\rm Tot}R_{\rm load}\,(L_{\rm in} - L_m)} \tag{A.5}$$

$$a_{dxi0} = \frac{(L_c + 2L_{\rm in} - L_m)\,(L_c + L_m)\left(R_{\rm in} + (1-D)^2 R_{\rm load}\right)}{C_o\,L_{\rm Tot}R_{\rm load}\,(L_{\rm in} - L_m)} \tag{A.6}$$

$$b_1 = \frac{\left(L_{\rm Tot} + 2C_o\,(L_c + L_m)\,R_{\rm in}R_{\rm load}\right)}{C_o\,L_{\rm Tot}R_{\rm load}} \tag{A.7}$$

$$b_0 = \frac{2\,(L_c + L_m)\left(R_{\rm in} + (1-D)^2 R_{\rm load}\right)}{C_o\,L_{\rm Tot}R_{\rm load}}. \tag{A.8}$$

REFERENCES

[1] O. Garcia, P. Zumel, A. De Castro, and J. A. Cobos, "Automotive DC-DC bidirectional converter made with many interleaved buck stages," *IEEE Trans. Power Electron.*, vol. 21, no. 3, pp. 578–586, May 2006.

[2] G. Calderon-Lopez and A. J. Forsyth, "High power density DC-DC converter with SiC MOSFETs for electric vehicles," in *Proc. IET Int. Conf. Power Electron. Mach. Drives*, 2014, pp. 1–6.

[3] N. Liqin, D. J. Patterson, and J. L. Hudgins, "High power current sensorless bidirectional 16-phase interleaved DC-DC converter for hybrid vehicle application," *IEEE Trans. Power Electron.*, vol. 27, no. 3, pp. 1141–1151, Feb. 2012.

[4] G. Calderon-Lopez, A. J. Forsyth, and D. R. Nuttall, "Design and performance evaluation of a 10-kW interleaved boost converter for a fuel cell electric vehicle," in *Proc. CES/IEEE 5th Int. Conf. Power Electron. Motion Control*, 2006, pp. 1–5.

[5] K. Hongrae, M. Falahi, T. M. Jahns, and M. Degner, "Inductor current measurement and regulation using a single DC link current sensor for interleaved DC-DC converters," *IEEE Trans. Power Electron.*, vol. 26, no. 5, pp. 1503–1510, Jun. 2011.

[6] J. Abu-Qahouq, M. Hong, and I. Batarseh, "Multiphase voltage-mode hysteretic controlled DC-DC converter with novel current sharing," *IEEE Trans. Power Electron.*, vol. 19, no. 6, pp. 1397–1407, Nov. 2004.

[7] J. Cabiles-Magsino, R. C. Guevara, and M. Escoto, "Implementation of sliding mode control for current sharing in fixed frequency voltage regulator modules," in *Proc. IEEE Region Conf. TENCON*, 2012, pp. 1–6.

[8] H. Xudong, W. Xiaoyan, T. Nergaard, L. Jih-Sheng, X. Xingyi, and L. Zhu, "Parasitic ringing and design issues of digitally controlled high power interleaved boost converters," *IEEE Trans. Power Electron.*, vol. 19, no. 5, pp. 1341–1352, Sep. 2004.

[9] O. Hegazy, J. Van Mierlo, and P. Lataire, "Analysis, modeling, and implementation of a multidevice interleaved DC/DC converter for fuel cell hybrid electric vehicles," *IEEE Trans. Power Electron.*, vol. 27, no. 11, pp. 4445–4458, Jun. 2012.

[10] D. De, C. Klumpner, C. Patel, K. Ponggorn, M. Rashed, and G. Asher, "Modelling and control of a multi-stage interleaved DC-DC converter with coupled inductors for super-capacitor energy storage system," *IET Power Electron.*, vol. 6, pp. 1360–1375, Sep. 2013.

[11] L. Yean-Kuo, S. Yi-Ping, H. Yu-Ping, L. Yu-Huei, C. Ke-Horng, and H. Wei-Chou, "Time-multiplexing current balance interleaved current-mode boost DC-DC converter for alleviating the effects of right-half-plane zero," *IEEE Trans. Power Electron.*, vol. 27, no. 9, pp. 4098–4112, May 2012.

[12] H. B. Shin, E. S. Jang, J. G. Park, H. W. Lee, and T. A. Lipo, "Small-signal analysis of multiphase interleaved boost converter with coupled inductors," *Proc. IEE Elect. Power App.*, vol. 152, pp. 1161–1170, Oct. 2005.

[13] S. K. Mazumder, "Stability analysis of parallel DC-DC converters," *IEEE Trans. Aerosp. Electron. Syst.*, vol. 42, no. 1, pp. 50–69, Mar. 2006.

[14] A. J. Forsyth and G. Calderon-Lopez, "Sampled-data analysis of the dual-interleaved boost converter with interphase transformer," *IEEE Trans. Power Electron.*, vol. 27, no. 3, pp. 1338–1346, Mar. 2012.

[15] D. M. VandeSype, K. DeGusseme, F. M. L. L. DeBelie, A. P. VandenBossche, and J. A. Melkebeek, "Small-signal z-domain analysis of digitally controlled converters," *IEEE Trans. Power Electron.*, vol. 21, no. 2, pp. 470–478, Mar. 2006.

[16] S. Buso and P. Mattavavelli, *Digital Control in Power Electronics*. San Rafael, CA, USA: Morgan & Claypool, 2006.

[17] B. C. Kuo, "Transfer functions, block diagrams and signal flow graphs," in *Digital Control Systems*, 2nd ed. USA: Oxford Univ. Press, 1992, ch. 4, sec. 7, pp. 149–167.

[18] J. T. Tuo, *Digital and Sampled-Data Control Systems*. New York, NY, USA: McGraw-Hill, 1959.

Alejandro Villarruel-Parra (M'08) received the B.Sc. degree in communications and electronics engineering, and the M.Sc. degree in microelectronics engineering from the National Polytechnic Institute (IPN), Mexico City, Mexico, in 2008 and 2010, respectively, and the Ph.D. degree in electrical and electronic engineering from the University of Manchester, Manchester, U.K. in 2015.

He is currently a Research Associate at the IPN. His research interests include control, modeling, and design of dc–dc converters, multilevel converters, and digital control of power electronics.

Andrew J. Forsyth (M'98–SM'06) received the B.Sc.(Eng) degree from Imperial College, London, U.K., in 1981, and the Ph.D. degree from the University of Cambridge, Cambridge, U.K., in 1987.

He was a Design Engineer with GEC Electrical Projects, Ltd., from 1981 to 1983, a Lecturer with the University of Bath from 1986 to 1990, and a Lecturer/Senior Lecturer with Birmingham University from 1991 to 2004. Since 2004, he has been a Professor of power electronics at the University of Manchester, Manchester, U.K. His research interests include high-frequency converters, high-frequency magnetic components, modeling, control, and energy storage, particularly for aerospace and electric vehicle applications.